Thermal entrainment and melting in mantle plumes

Dinzia G. Farnetani, Mark A. Richards *

Department of Geology and Geophysics, University of California, Berkeley, CA 94720 , USA

Abstract

Thermal plumes from the core–mantle boundary (CMB) are thought to cause volcanic hotspots, and starting plumes, or plume 'heads', are thought to cause voluminous flood basalt events at the beginning of some hotspot tracks. It has been proposed that starting plumes entrain a large volume fraction of surrounding mantle material as they rise from the CMB to the base of the lithosphere, and that this process of thermal entrainment can explain some aspects of isotope and trace element heterogeneity in hotspot and flood basalt lavas. We examine this hypothesis using numerical models of mantle plumes generated by a thermal boundary layer at the base of the mantle. Our numerical experiments are designed to simulate plumes with characteristics appropriate to explain major hotspots such as Hawaii. The flow trajectory of original plume source (boundary layer) material is mapped using a neutral buoyancy chemical tracer field. We incorporate a simple parameterized batch melting model in order to examine in detail the proportion of different mantle components ('enriched' boundary layer vs. 'depleted' ambient mantle) which undergo partial melting as starting plumes spread beneath the lithosphere. The effects of a variety of physical model parameters are explored, including temperature and depth-dependent viscosity, and phase changes in the mantle transition zone. In all cases, we find little entrainment of surrounding mantle into the region of the plume head that undergoes a significant degree of partial melting, so that the primary plume magmas represent > 90% original plume source material. These results suggest that hotspot lavas do not sample a large volume fraction of the mantle through which plumes rise, in apparent disagreement with previous interpretations of laboratory experiments on thermal entrainment in plumes. The differences arise because: (1) we examine entrainment in the melting region, rather than the entire plume head; (2) our plumes arise naturally from a boundary layer, which imposes an initial thermal gradient from plume center to periphery; (3) starting plumes in the mantle rise only about 3 plume head diameters before spreading ('unwrapping') and melting beneath the lithosphere; and (4) we have modeled cases in which plumes melt at sublithospheric depths, without large-scale lithospheric extension. We suggest that geochemical heterogeneity in hotspot and flood basalt lavas is mainly a reflection of either inherent plume source heterogeneity or contamination from the crust and lithosphere through which primary magmas rise.

1. Introduction

Intraplate volcanic hotspots are probably generated by plumes of hot material rising from the

Earth's deep mantle [1,2]. It is also likely that continental flood basalts and oceanic plateaus are formed by enhanced melting of a large plume head at the initiation of mantle plume activity [3–6]. The geochemical signatures of hotspot lavas and of flood basalts are quite variable but they are generally enriched in incompatible elements relative to mid-

---

* Corresponding author.

ocean ridge basalts (e.g. [7,8]). This difference suggests that deep mantle plumes may replenish the geochemically depleted upper mantle with an enriched component [9]. The geochemical signature of plume volcanism cannot be explained entirely by crustal and lithospheric contamination or partial melting but, instead, seems to require an enriched mantle source. Moreover, thermal models suggest that melting of the lithosphere is minimal and that the bulk of primary magmas are produced within the mantle plume [10–12]. Mantle plumes and their leading head are also thought to be geochemically heterogeneous. The heterogeneities may be directly inherited from the deep mantle source, or they may develop dynamically by entrainment [13]. In the latter case distinct geochemical components are stirred together by solid-state flow in the plume.

In the last decade entrainment in mantle plumes has been studied with laboratory experiments (e.g., [13,14]), which show that a thermally buoyant plume conductively heats and entrains the adjacent fluid as it ascends. The laminar stirring of surrounding fluid has two effects: it cools and enlarges the plume and it generates a geochemical zonation in the plume head. The compositional differences between the original source material and the entrained mantle are stirred but they are not thoroughly mixed, due to the negligible rate of chemical diffusion [13]. Laboratory experiments indicate that entrainment is a significant phenomenon for thermally buoyant plumes [13], for isolated thermal diapirs [14] and for steady-state conduits [15–17], while it may be negligible for chemically buoyant plumes [18,19]. These experiments have been very influential in our understanding of plume dynamics but they have several important limitations. First, they do not include any melting model; thus, it is impossible to investigate the extent of melting of the entrained material. The second limitation of many laboratory experiments is that the plumes are fed from a continuous 'point source' of buoyant fluid, and plumes do not form naturally as thermal boundary layer instabilities.

In this paper we present results from numerical models of mantle plume dynamics in which we focus on the degree of chemical entrainment between thermally buoyant deep-source material and the surrounding mantle. Our finite element model solves for the dynamics of solid-state convection and for the

advection of a neutrally buoyant tracer field. The tracer field, or concentration field (hereafter called the C-field), represents the original plume source material (in the boundary layer), which we take to have the geochemical signature of 'enriched' deep mantle. The C-field allows us to track the source material which initially fills the thermal boundary layer, ~ 100 km thick, at the bottom of the mantle. The plume grows as a boundary layer instability and we model the entrainment of surrounding mantle as the plume rises to the surface. We also investigate the effects of variable viscosity structure (e.g., isoviscous, layered and temperature-dependent viscosity) and solid–solid phase transitions on plume dynamics and on entrainment. The numerical code includes an anhydrous batch melting model to define the melting zone, which allows us to quantify the degree of entrainment in the region undergoing partial melting. Moreover, we estimate the trace element concentrations and isotope ratios of partial melts by assuming initial concentrations for two 'end members' (i.e., the depleted surrounding mantle and the primitive source material). Our results consistently show that the melting of entrained material contributes little to the total melt production (less than 10%), thus suggesting that magmatic products of mantle plumes, fed naturally from a thermal boundary layer, are unlikely to reflect much entrainment from the mantle through which they rise.

2. The numerical model

We used a two-dimensional finite element code (ConmanCYL, [12]) in cylindrical geometry to investigate the dynamics of geochemical entrainment in thermally buoyant plumes. The code solves simultaneously the advection–diffusion equations for a Newtonian, incompressible viscous fluid and the advection equation governing the flow of a neutrally buoyant chemical field. In non-dimensional form the governing equations are:

Incompressibility

$$\nabla \cdot U = 0 \tag{1}$$

Conservation of momentum at infinite Prandtl number

$$-\nabla_p + \nabla^2 U + RaT\hat{z} = 0 \tag{2}$$

Table 1
Model parameters and physical constants

Symbol	Model parameter	Value
d	Dimensional depth of the cylinder	2900 km
ΔT	Potential temperature contrast across the lithosphere	1300 °C
δT	Potential temperature contrast across the box	1700 °C
g	Gravitational acceleration	10 m s^{-2}
κ	Thermal diffusivity	10^{-6} m^2 s^{-1}
η	Mantle viscosity	3×10^{21} Pa s
α	Thermal expansion coefficient	3 ×10^{-5} °C^{-1}
ρ	Mantle density	3500 kg m^{-3}
$\rho_{660}=\rho_{410}$	Mantle density at 660 and 410 km depth	3500 kg m^{-3}
$\Delta\rho_{660}=\Delta\rho_{410}$	Density contrast between phases	350 kg m^{-3}
γ_{660}	Clapeyron slope at 660 km depth	-3 MPa/°K
γ_{410}	Clapeyron slope at 410 km depth	3 MPa/°K
h	Thickness of phase transition	2×10^4 m
K	Thermal conductivity	4.2 W m^{-1}°K^{-1}
ΔS	Entropy of fusion	400 J kg^{-1}°K^{-1}
C_p	Specific heat at constant pressure	1.2×10^3 J kg^{-1}°K^{-1}

where U = the velocity vector; T = potential temperature; t = time, p = the dynamic pressure and $\check{z}$ is a unit vector in the vertical direction. The equations are nondimensionalized by scaling the distance according to the cylinder depth, d; temperature according to the temperature contrast ΔT across the lithosphere; and time according to d^2/κ where κ is the thermal diffusivity. Numerical values of the scaling parameters are given in Table 1. All material properties are combined in the Rayleigh number:

$$Ra = \frac{g\alpha\rho\delta T d^3}{\kappa\eta} \qquad (3)$$

where δT is the potential temperature contrast across the box.

Conservation of energy is given by:

$$\frac{\partial T}{\partial t} + (\nabla T)\cdot U = \nabla^2 T \qquad (4)$$

Chemical differences are represented by a continuous function, which gives the concentration of the original source material. The flow of the neutrally buoyant chemical field (the C-field) is described by an advection equation:

$$\frac{\partial C}{\partial t} + (\nabla C)\cdot U = \frac{1}{Le}\nabla^2 C \qquad (5)$$

in which we add a small diffusive term. Although the chemical diffusivity of materials is many orders of

magnitude less than the thermal diffusivity, we use a Lewis number $Le = 100$ [20], (Le = thermal diffusivity/chemical diffusivity). Following the advection of a sharp interface requires the use of a small chemical diffusivity to reduce numerical diffusion, which falsely enhances mixing whenever the tracer field is treated as a continuous field [21]. We also partially correct for this spurious diffusion by applying the algorithm of Lenardic and Kaula [22]. Nonetheless, our calculations suffer from some degree of numerical diffusion, and this effect tends to result in more apparent mixing or entrainment, rather than less.

The size of the finite element box is 1740 km in radius and 2900 km in depth, and we use a non-uniform Eulerian grid of rectangular elements (92 × 159). The radius of the elements is $17 \le r_e \le 27$ km and the height is $15 \le z_e 20$ km, with the smaller elements closer to the axis of symmetry. A more complete description of the code, the equation solver, and the implementation of the melting model are given in [12].

2.1. Melting model and geochemical mixing

The code uses the anhydrous batch melting model of McKenzie and Bickle [23] to calculate melt fraction and major element concentration in the melt. Melting affects the temperature field through the absorbtion of latent heat, which is estimated using a constant entropy of fusion ($\Delta S = 400$ J kg^{-1}°K^{-1}, appropriate for a mantle potential temperature $T_{Pm} = 1300$°C). The melt fraction and the melt production rate are calculated at each node and at each time step, along with the value of the C-field. The C-field gives the proportion of chemical mixing between primitive source material and entrained mantle. Having the melt fraction (X) and the proportion of plume source versus entrained mantle, we can estimate trace element concentrations and isotope ratios in the primary melts, following Ribe's formulation [24]. We first calculate the trace element concentration for batch melting of the plume source component, $c_s = c_{0s}/K_D + X(1 - K_D)$ and of the entrained component, $c_m = c_{0m}/K_D + X(1 - K_D)$, where c_{0s} and c_{0m} are the trace element concentration in the unmelted source rock and in the entrained material, respectively, and K_D is the partition coefficient for each

element. The representative values used are given in Table 2. These relations contain the implicit assumptions that the degree of melting is equal in the enriched and depleted components, and that the melt does not segregate from its mantle source. We then calculate the concentration ratio of two trace elements in the liquid:

$$\frac{C_l^1}{C_l^2} = \frac{(q_s c_s + q_m c_m)_1}{(q_s c_s + q_m c_m)_2} \tag{6}$$

and the isotope ratio in the liquid:

$$\eta = \frac{(q_s c_s r_s + q_m c_m r_m)}{(q_s c_s + q_m c_m)} \tag{7}$$

In the above equations r_s and r_m are the isotope ratio in the plume source and in the entrained component given in Table 2, respectively. The melt production in the plume source: $q_s(r,z,t) = X(r,z,t) \times (C(r,z,t)/100)$ is calculated at each node and at each time step by 'weighting' the melt fraction with the corresponding value of the concentration field. The melt production of the entrained mantle $q_m(r,z,t) = X(r,z,t) \times (1 - C(r,z,t)/100)$ is similarly defined. (The factor of 100 appears because C is represented in percent. Note also that $X(r,z,t)$ is identical in q_s and in q_m, thus this term cancels in Eqs. 6 and 7).

2.2. Initial and boundary conditions

Our initial and boundary conditions are designed to model a narrow upwelling plume from a boundary layer at the bottom of the mantle, which supplies a

heat flux, sufficient to account for the Hawaiian hotspot, which is probably the largest mantle plume. The heat flux at Hawaii is of order 1% of the total mantle heat flux, or about 1/5th to 1/15th of the heat flux from the core–mantle boundary, assuming that the total heat flux from all plumes constitutes about 5–15% of the mantle heat flux [25,26]. Thus, a plausible scenario is that the Hawaiian plume 'drains' about 1/15th of the area of the core–mantle boundary, which leads us to choose the radius of our cylindrical box to be 1740 km.

By further specifying reasonable choices for the depth, viscosity, density, thermal diffusivity, thermal expansivity and the potential temperature (i.e., the temperature that the material would have if brought adiabatically to the Earth's surface) $T_{Pm} = 1300°C$ for the mantle, and $T_{Ps} = 0°C$ for the upper surface, we are left to choose a bottom potential temperature ($T_{Pb} = T_{Pm} + \Delta T_b$) that will supply an appropriate heat flux.

With the parameters of Table 1 and a mantle viscosity of 3×10^{21} Pa s, a good guess for the bottom boundary temperature can be made through the standard Nusselt number–Rayleigh number relationship for bottom-heated convection: $Nu = 0.225 Ra^{-1/3}$ [27]; where $Nu = Q/Q_c$. Q_c is the heat flow rate through the mantle by conduction, and Q is the heat flow rate by convection. Using $Q \sim 2.6 \times 10^{11}$ W ($\sim 1\%$ of the mantle heat flux), we estimate that $\Delta T_b = 400°C$, or $T_{Pb} = 1700°C$. This estimate does, in fact, produce a plume of the desired strength (heat flux) in our models. These choices result in a Rayleigh number (see Eq. 3) $Ra = 1.1 \times 10^7$.

Table 2
Trace element concentration

Element or ratio	Value in plume source [1]	Value in entrained material [2]	Partition coefficient
Sr	23.7 ppm	13.2 ppm	0.008
Nd	1.2 ppm	0.86 ppm	0.03
La	0.71 ppm	0.31 ppm	0.0025
Ce	1.9 ppm	0.95 ppm	0.005
$^{87}Sr/^{86}Sr$	0.7047	0.7023	
$^{143}Nd/^{144}Nd$	0.51265	0.51330	

Values from [33]: [1] for undepleted mantle; [2] for MORB source.

An alternative approach to the one outlined above would be to first choose a CMB temperature contrast, and then choose a mantle viscosity to yield the appropriate heat flux. Larger values for temperature contrast result in smaller viscosities, and vice versa. A temperature contrast of $\Delta T_b = 400°C$ is a reasonable estimate for the temperature drop across the CMB, and this value also leads to melt volumes that are of the order observed in flood basalt events (see Results section).

In order to speed up our calculations, we set up an initial temperature distribution at the bottom of the box that is appropriate for a boundary layer at $Ra = 1.1 \times 10^7$. The temperature decreases from T_{Pb} to T_{Pm} as an error function profile over a thermal boundary layer of initial thickness $\delta = K \Delta T_b / Q$, where K is the thermal conductivity. The initial thickness of the thermal boundary layer is about 100 km. We also apply a small temperature perturbation (0.2% of the mantle temperature) at the top of the thermal boundary layer in order to trigger a thermal instability along the axis of symmetry. These initial and boundary conditions result in a plume of appropriate strength that grows naturally as a boundary layer instability.

The initial condition for the C-field is a 100 km thick layer at 2900 km depth which is geochemically distinct from the overlying mantle. The initial concentration throughout this layer is $C_0 = 100$, which represents a concentration of 100% original source material. For the entire mantle above $C_0 = 0$. All boundaries for the C-field are closed, since there is no flux of tracer through the boundaries. For these models we have assumed that the chemical and the thermal boundary layers have the same thickness.

The velocity boundary conditions are appropriate for a model with an old, non-rifting lithosphere. At the surface we impose zero vertical and radial velocity components ($U_z = 0 = U_r$). To model a non-rifting lithosphere the radial velocity is set to zero from the surface to 40 km depth, a representative elastic thickness for an old oceanic lithosphere. The effect of different top boundary conditions on the depth and amount of melting within the plume head has been investigated in previous models [12]. On the bottom boundary we impose zero vertical velocity and radial free slip ($U_z = 0 = \partial U_r / \partial_z$), while along the axis of symmetry and the right side of the box, we impose zero radial velocity and vertical free slip ($U_r = 0 = \partial U_z / \partial r$).

2.3. Mantle phase transitions

The code calculates how the endothermic and exothermic phase transitions, at 660 and 410 km depth, respectively, affect flow and geochemical entrainment. Although solid–solid transitions in the mantle are likely to be polyvariant in nature [28], a univariant phase change is an acceptable approximation, as indicated by the sharpness of phase transitions [29]. In such a case, the Clapeyron slope provides a unique relation between pressure and temperature. The location of the phase boundary is expressed by the phase function, Γ, which gives the relative fraction of the heavier phase ($0 \le \Gamma \le 1$). The phase function depends upon pressure and temperature through a hyperbolic tangent function [30]. For the endothermic phase change:

$$\Gamma_{660} = \frac{1}{2}\left[1 + \tanh\left(\frac{P - P_{660} - \gamma_{660}\left(\overline{T} - \overline{T}_{660}\right)}{\rho_{660}^{gh}}\right)\right]$$

(8)

where $\overline{T}_{660}$ and P_{660} are the ambient real temperature and the lithostatic pressure at 660 km depth, while $\overline{T}$ and P are the real temperature and lithostatic pressure at each node. The temperatures are converted from potential (T_p) to real ($\overline{T}$), assuming an adiabatic gradient, so that $< \overline{T} = T_p \exp(g \alpha z / C_p)$, while the lithostatic pressure is defined as $P = \rho g z$ (Note that Γ_{410} is similarly defined as (8)). The Clapeyron slope is chosen to be $\gamma_{660} = -3$ MPa/°K, a value which is representative of experimental and seismological estimates [29]. At 410 km depth, we use $\gamma_{410} = 3$ MPa/°K.

Due to the different densities of two phases a buoyancy force is associated with the deflection of the phase boundary. If the phase boundary is deflected upward by the plume (negative Clapeyron slope) the buoyancy force hinders the ascent of the plume. For a downward deflection (positive Clapeyron slope) the buoyancy force enhances the ascent. We include the buoyancy forces in the conservation of momentum equation by adding the term:

$$Ra\left(-R_{660}\Gamma_{660} + R_{410}|\Gamma_{410} - 1|\right)\hat{z}$$

(9)

to the left side of (2). The dimensionless coefficients $R_{660} = \Delta\rho_{660}/\alpha\Delta T\rho$ and $R_{410} = \Delta\rho_{410}/\alpha\Delta t\rho$ are proportional to the density change due to the phase transition. A phase change also effects the buoyancy through the release/absorbtion of latent heat, which is included in the energy equation by adding the term:

$$R_{T_{660}}\left[\frac{\partial \Gamma_{660}}{\partial t} + (\nabla\Gamma_{660}) \cdot U\right]$$

$$+ R_{T_{410}}\left[\frac{\partial \Gamma_{410}}{\partial t} + (\nabla\Gamma_{410}) \cdot U\right] \tag{10}$$

to the right side of (4). The dimensionless coefficients $R_{T_{660}} = q_{L_{660}}/C_p\Delta T$ and $R_{T_{410}} = q_{L_{410}}/C_p\Delta T$
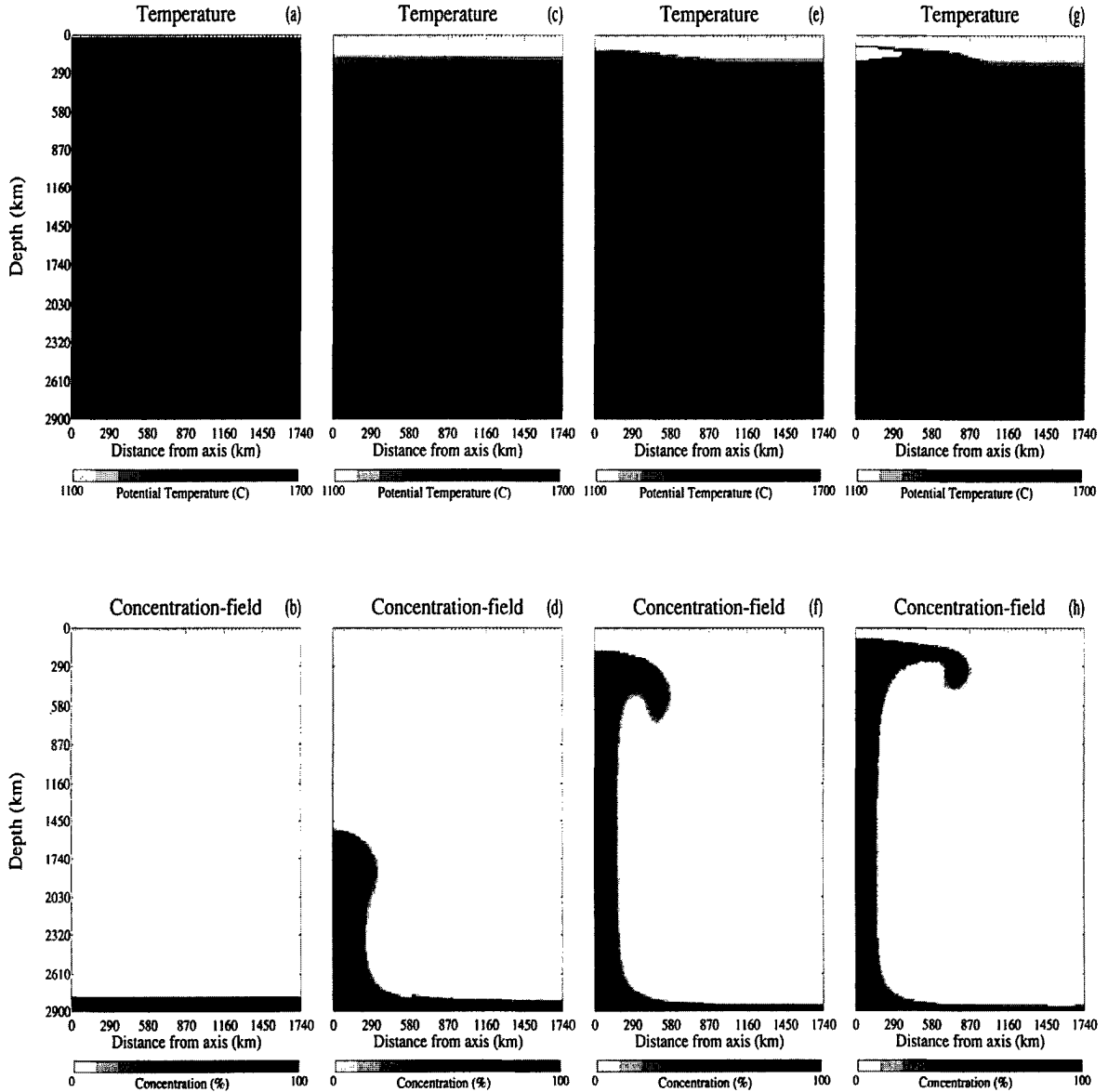
Fig. 1. Evolution of a plume for the model with an isoviscous mantle. Top: the temperature field. (a) The initial condition, (c), (e), (g) later stages. In (g) the melting zone is the white area beneath the lithosphere. Bottom: the Concentration field. (b) The initial condition, (d), (f), (h), later stages, at the same elapsed time as for the temperature field. The scale for the C-field is from 0 to 100%, see text. To show the temperature structure of the plume more clearly, the minimum potential temperature in the gray scale is 1100°C. This means that the lithosphere, (where $T < 1100°C$) is depicted in white.

are directly proportional to the energy released per unit mass during the phase change ($q_{L_{660}} = \gamma_{660}(\overline{T} - \overline{T}_m) \Delta\rho_{660}/\rho^2$ ($q_{L_{410}}$ similarly defined). Note that energy released per unit mass is proportional to the real temperature difference between the plume and the ambient mantle at the same depth ($\overline{T}_m$).

2.4. Mantle viscosity models

Our reference model has a uniform viscosity for the mantle and the lithosphere ($\eta_m = \eta_{lith} = 3 \times 10^{21}$ Pa s). We also consider a model with a ten-fold

increase in viscosity between upper and lower mantle (i.e., $\eta_{um} = 10^{21}$ Pa s, and $\eta_{lm} = \eta_{lith} = 10^{22}$ Pa s). For the case with temperature-dependent viscosity we use the exponential law:

$$\eta(T) = \eta_m \exp(-b(T-1)) \qquad (11)$$

where $\eta_m = 3 \times 10^{21}$ Pa s is the reference mantle viscosity at potential temperature $T_{Pm} = 1300°C$, $b = 10.97$ is a constant, and T is the nondimensional potential temperature. This law gives a dynamic viscosity contrast of 30 between the surrounding mantle and the plume for a plume excess tempera-
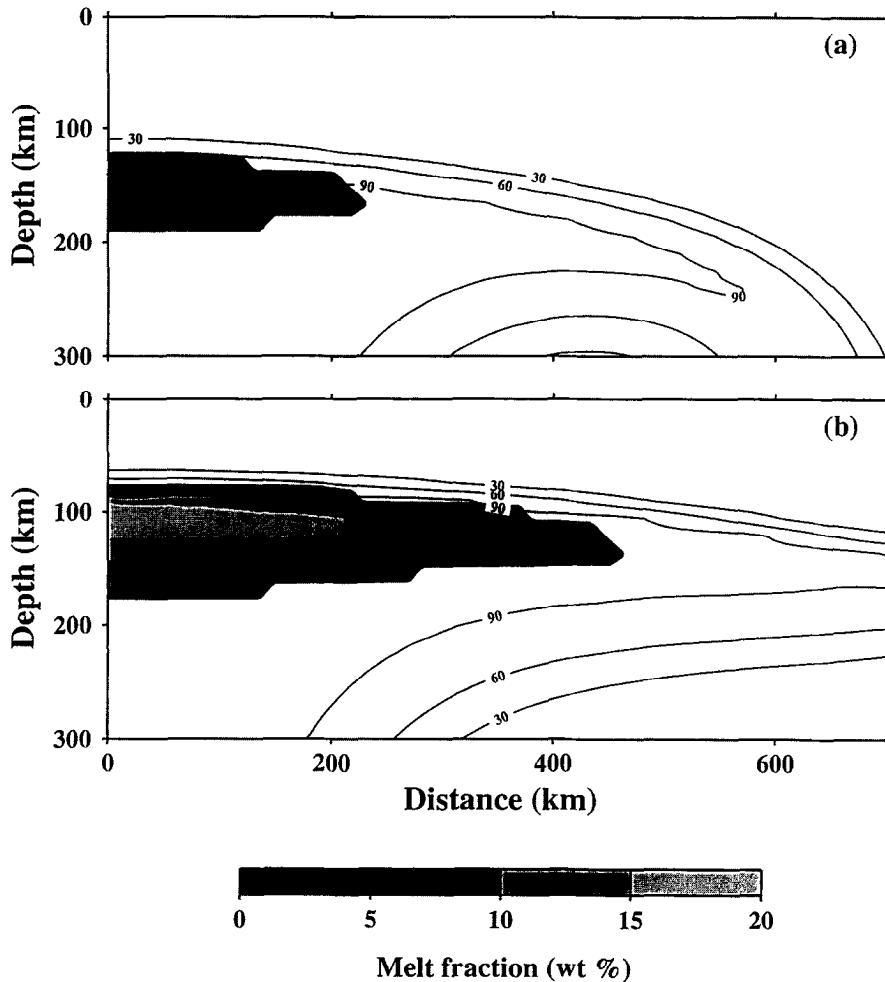

Fig. 2. Model with isoviscous mantle: contours of the concentration field. The melting region is shaded. (a) At the onset of melting. (b) After 15 Myr. (The unsmoothed shape of the melting region reflects the grid spacing (i.e., ~ 17 × 15 km) at lithospheric depths).

ture of 400°C. This viscosity ratio is modest compared to estimates for olivine rheology but it is used because it guarantees good resolution; for the same reason we also set an upper bound on the viscosity at lower temperatures, so that $\eta_{max} = 3 \times 10^{22}$ Pa s. In our model the viscosity of the lithosphere is two orders of magnitude smaller than some estimated values; however, deformation in the upper 40 km is prevented by the non-rifting boundary condition.

3. Results

3.1. The reference model

The reference model has uniform mantle viscosity ($\eta_m = 3 \times 10^{21}$ Pa s) and does not include phase transitions. The initial conditions described in the previous section are illustrated in Fig. 1a for the temperature field and in Fig. 1b for the C-field. Within the layer of plume source material C = 100, while in the overlying mantle C = 0 (Fig. 1b). The chemical layer also corresponds to the thermal boundary layer, which has a temperature contrast of 400°C (Fig. 1a). The plume develops as a thermal boundary layer instability, and after approximately 160 Myr the head is at 1600 km depth (Fig. 1c). The

plume has not developed a large spherical head and the ratio of head/tail radius, calculated for the 1500°C isotherm, is less than 2. This is expected, since the model is isoviscous. At the top boundary, the cooling boundary layer develops a temperature profile of the error function form for 160 Myr old oceanic lithosphere. The C-field (Fig. 1d) indicates that the original source material is swept into the rising plume, and there is very little entrainment of surrounding mantle into the plume head.

In Fig. 1e (the time interval between Fig. 1c and e is 20 Myr) the plume is at 300 km depth and has a radius of 500 km, if we consider the 1500°C isotherm as a reference. The hottest part along the axis has an excess temperature greater than 350°C. The corresponding C-field (Fig. 1f) indicates that the degree of entrainment within the head is negligible. The zones with higher degree of entrainment are concentrated around the plume and they do not recirculate within the head. As the plume rises to shallower depths the head spreads radially beneath the lithosphere. Fig. 1g (15 Myr after Fig. 1e) shows the temperature field and the corresponding melting region (in white), partial melting occurs at sublithospheric depths in the plume head, where the excess temperature is ~ 330°C. The corresponding C-field (Fig. 1h) shows that the material which is hot enough to melt has
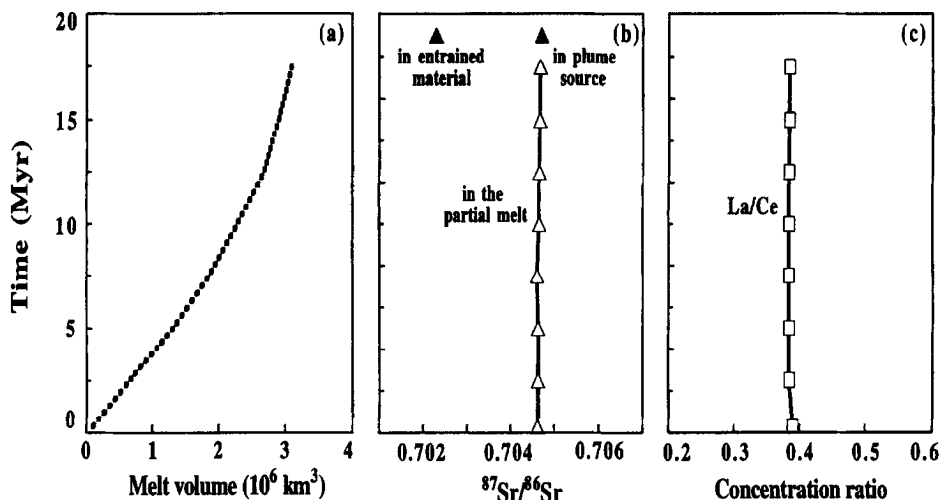

Fig. 3. Model with isoviscous mantle. (a) Melt volume as a function of time after the onset of melting. (b) Calculated ^{87}Sr/^{86}Sr ratio in the partial melt. (c) Calculated La/Ce ratio in the partial melt.

very high concentrations of source material (C > 90%), while parts of the plume that entrained more surrounding mantle have temperatures below the calculated solidus.

Fig. 2 shows contours of the concentration field and the melting region (shaded), at the onset of melting (Fig. 2a), when the total melt volume is 0.4×10^6 km^3, and at a later stage (Fig. 2b), when
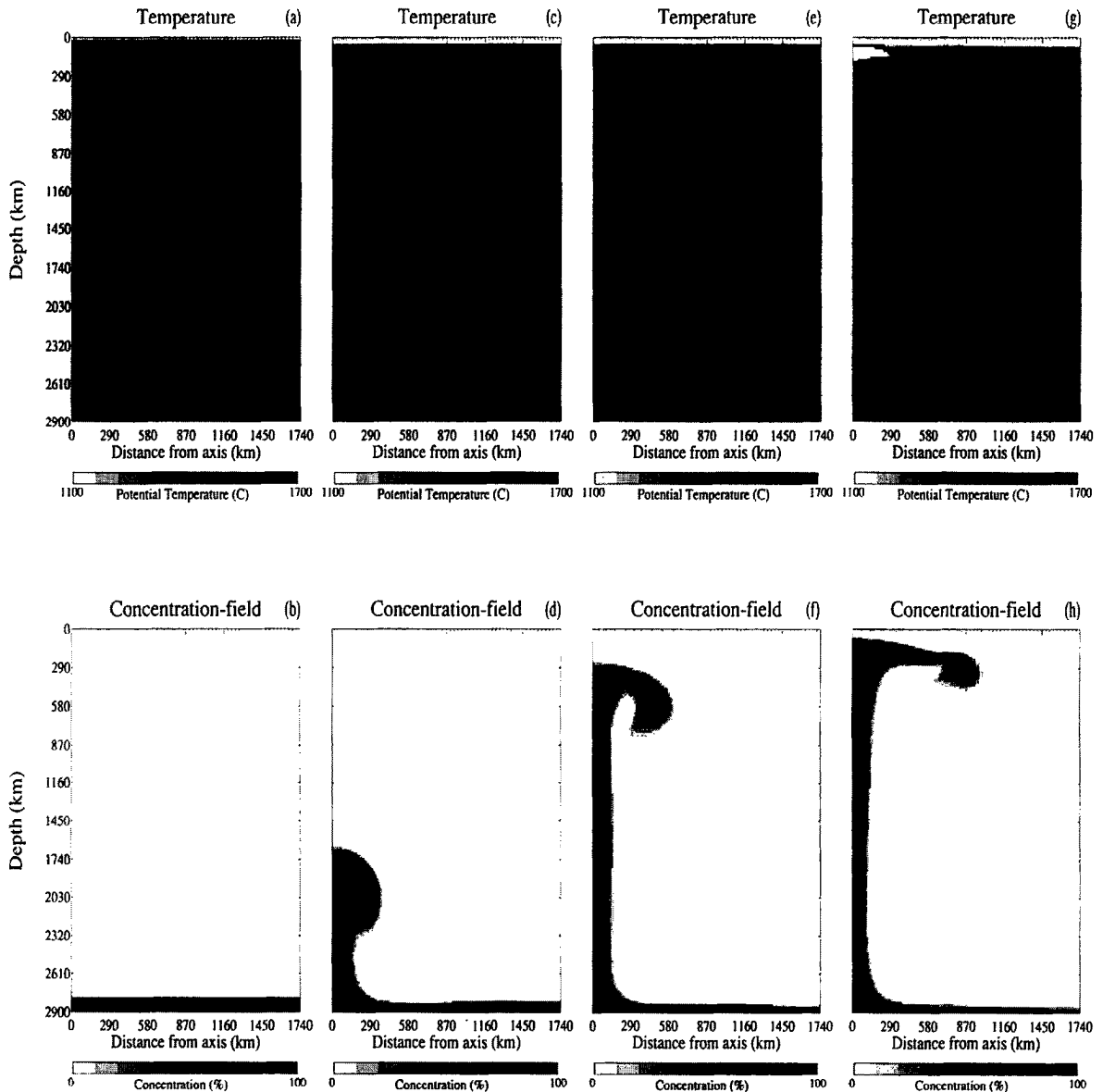

Fig. 4. Evolution of a plume for the model with temperature-dependent viscosity. Top: the temperature field. (a) The initial condition, (c), (e), (g) later stages. In (g) the melting zone is the white area beneath the lithosphere. Bottom: the concentration field. (b) The initial condition, (d), (f), (h), later stages, at the same elapsed time as for the temperature field. The scale for the C-field is from 0 to 100%, see text. To show the temperature structure of the plume more clearly, the minimum potential temperature in the gray scale is 1100°C. This means that the lithosphere (where $T < 1100$°C) is depicted in white.

the total melt volume is 3.1×10^6 km^3, in agreement with estimated volumes for continental flood basalt events. In Fig. 2a the melting region has a radial extent of 200 km and the melt fraction is everywhere less than 10 wt%. Partial melting occurs in the part of the plume head where the concentration of original plume source material is higher than 60%. Fig. 2b (after 16 Myr) shows that the plume head is at a shallower depth and has spread radially beneath the lithosphere. The melting region has a radius of 400 km and the highest melt fraction is 20 wt%. Also, in this case, the plume material partially melting has a high concentration of original plume source material (i.e., C-field > 80%). Thus, independently of the elapsed time after the onset of melting, partial melting occurs only in zones with higher temperatures and low degrees of entrainment. Overall, entrained material does not melt extensively, and the bulk of melt production comes from original plume source material. In our model the melt volume is calculated with a batch melting model that includes neither the effect of melt extraction nor the effect of the change in composition of the residual matrix as melting proceeds. However, the results on the degree of entrainment of the plume material undergoing partial melting are a weak function of the melt volume and of the particular melting model being used.

Fig. 3a shows the melt volume as a function of elapsed time after the onset of melting for the reference model. The total melt volumes of our reference model (ca. 3×10^6 km^3), and of the models to follow, bracket the range of expected melt volumes due to starting plumes. We also note that if we had allowed the lithosphere to spread, or 'rift,' the melt volume would have been almost an order of magnitude larger [12], as observed for the very largest oceanic flood basalt plateaus. Fig. 3b and c show, respectively, the calculated ^{87}Sr/^{86}Sr and La/Ce ratios in the primary melt as a function of time, for the reference model. Since the material partially melting has such a high concentration of the original plume source material, the isotope ratio is very close to the plume source end member, and it is essentially constant over time. Also, the average value for the ^{143}Nd/^{144}Nd ratio over the whole melting region (0.512677) is very similar to the ratio assumed for the plume source (0.51265). These example calculations are only indicative, since the assumption of a batch melting is probably inadequate for calculations of incompatible element concentrations.
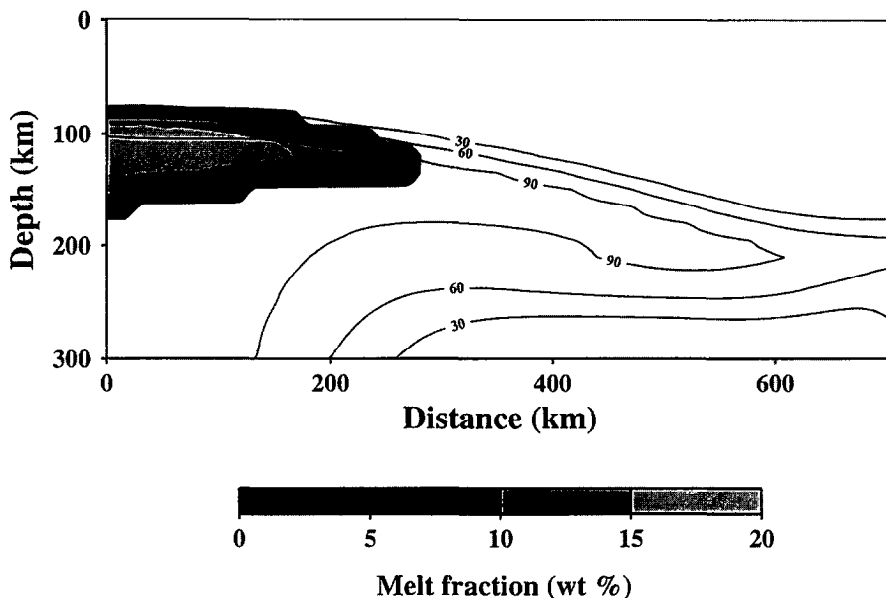

Fig. 5. Model with temperature-dependent viscosity: contours of the concentration field. The melting region is shaded.

3.2. Temperature-dependent viscosity model

In this model the viscosity of the plume (at $T_P = 1700°C$) is 30 times less than the reference mantle

viscosity ($\eta_m = 3 \times 10^{21}$ Pa s at $T_{Pm} = 1300°C$). The initial condition for the temperature and the C-field (Fig. 4a and b, respectively) are identical to the previous case. The reduced viscosity of the hot
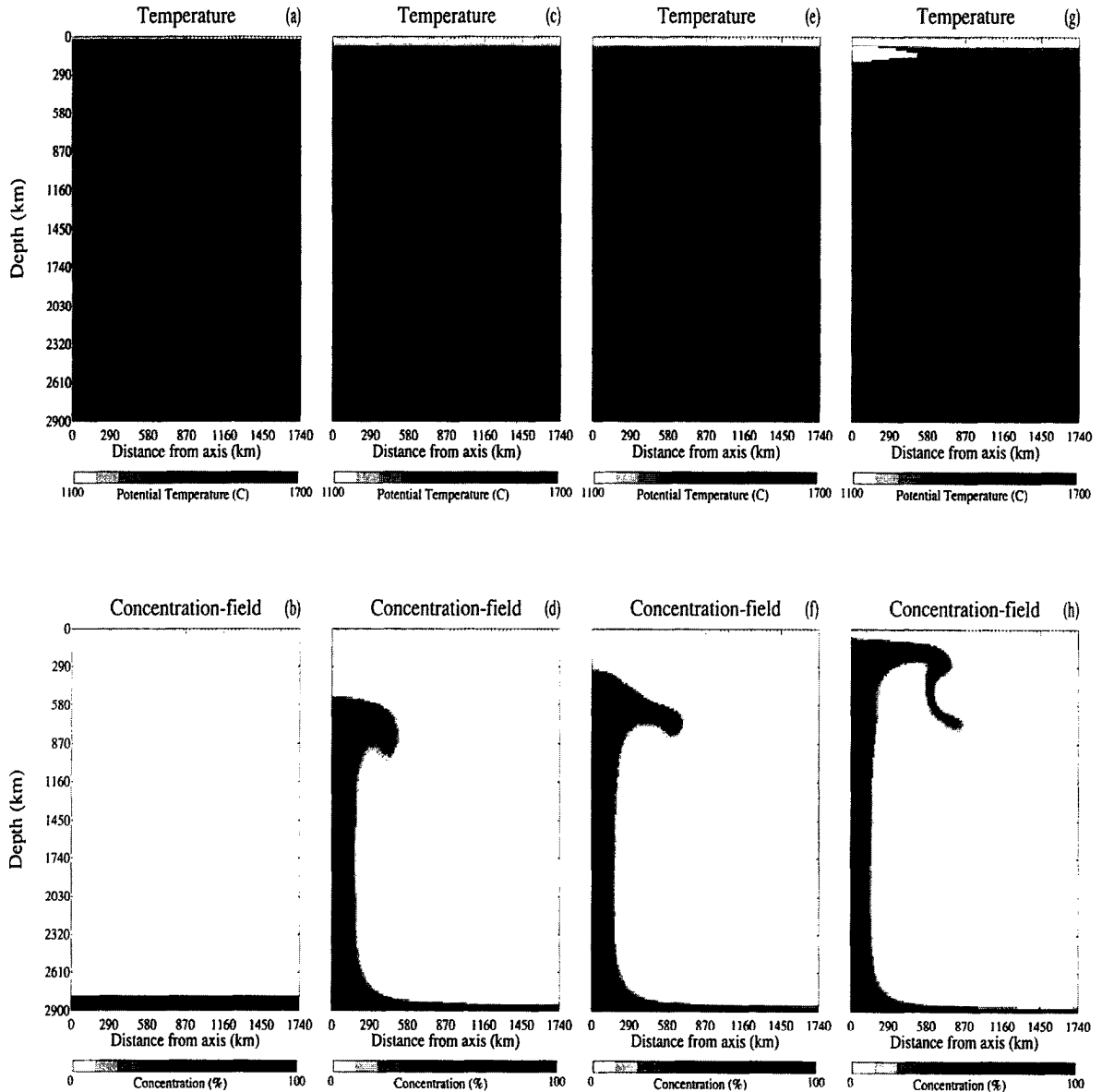

Fig. 6. Evolution of a plume for the model with phase transitions in an isoviscous mantle. Top: the temperature field. (a) The initial condition. (c) The plume at the endothermic phase change. (e) The plume ascending through the exothermic phase change. (g) The plume is at sublithospheric depths. In (g) the melting zone is the white area beneath the lithosphere. Bottom: the concentration field. (b) The initial condition, (d), (f), (h), later stages, at the same elapsed time as for the temperature field. The scale for the C-field is from 0 to 100%, see text. Note that, to show the temperature structure of the plume more clearly, the minimum potential temperature in the gray scale is 1100°C. This means that the lithosphere (where $T < 1100°C$) is depicted in white.

boundary layer enhances the formation and ascent of the plume and the head rises to 1600 km depth after only 70 Myr (Fig. 4c). The ratio of head to tail diameter is now greater than 4, using the 1500°C isotherm as a reference. The corresponding concentration field (Fig. 4d) shows that the surrounding mantle is dragged into the base of the plume cap between the stem and the outer part of the plume head. This flow pattern persists as the plume head rises and Fig. 4e (after 15 Myr) shows that the higher temperatures ($T > 1625$°C) are along the axis and within a torus-shaped volume at ~ 350 km radial distance. The corresponding C-field (Fig. 4f) indicates that the torus has a high concentration ($C > 90\%$) of original source material. However, neither the torus nor the mantle material surrounding it are wrapped within the plume head. Instead, they flow radially away from the axis, as the plume head spreads beneath the lithosphere. This 'unwrapping' due to shear flow in the spreading plume head serves to further confine melting to the high C-field material. The area partially melting (indicated in white in Fig. 4g) is within a radius of 300 km from the plume axis, and it has a high concentration of source material, as in the isoviscous case. We note that the torus

enriched in source material does not melt (Fig. 4h) and, thus, it may contribute to the geochemical heterogeneity of the upper mantle.

Fig. 5 shows contours of the C-field and the melt fraction, when the melt volume is $\sim 2 \times 10^6$ km^3. We also find in this case that, within the melting zone, the concentration of source material is higher than 90% and that zones of the plume head with more entrainment have temperatures below the solidus.

For this model we also calculate the buoyancy flux through the plume tail. This allows us to compare estimated plume fluxes for the Earth's mantle [25,26] to our model, which is designed to simulate plumes with characteristics appropriate to major hotspots, such as Hawaii. The buoyancy flux through the plume tail is $Q_b = Q_m \alpha \Delta T$, where: ΔT is the excess temperature integrated across the plume tail; $Q_m = Av\rho$ is the plume mass flux, A is the cross-sectional area of the plume conduit, α and ρ are given in Table 1, and v is the vertical velocity (the calculated rise velocity on the axis is of order 10–20 cm/yr). The plume boundary is defined where the excess temperature is 1% of the maximum excess temperature, using the Hauri at al. 'thermal halo'
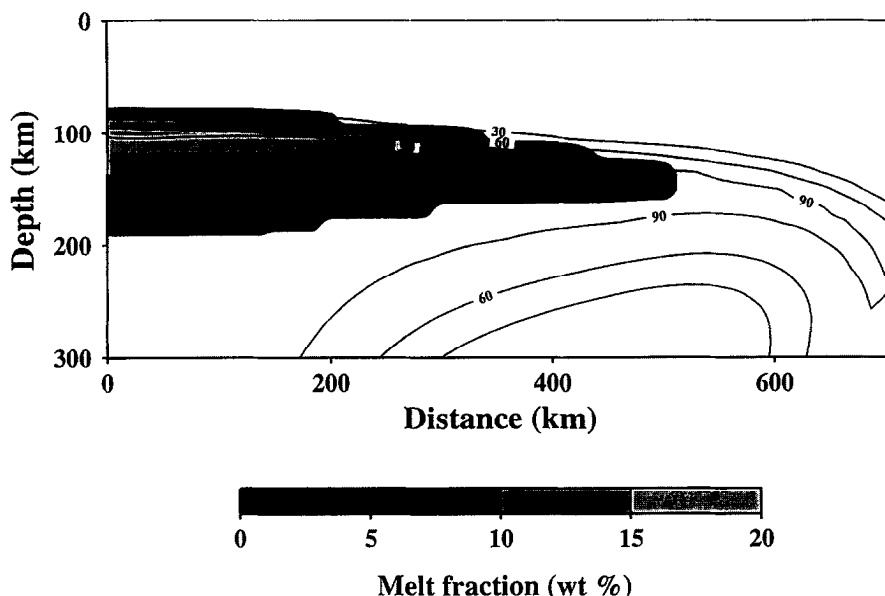

Fig. 7. Model with mantle phase transitions: contours of the concentration field. The melting region is shaded.

criteria [16]. The calculated buoyancy flux through the plume tail is 6–8 Mg/s, which is in agreement with calculated values for Hawaii (e.g., 8.7 Mg/s [26] and 6.3 Mg/s [25]) but is higher than estimates for Iceland (~ 1.4 Mg/s). We also find that, in the plume tail, more than 80% of the total buoyancy flux is due to plume material with a high concentration of source material (i.e., $C > 80\%$).

3.3. Model with mantle phase transitions

Our model allows us to investigate the effect of phase transitions on the degree of entrainment. The phase change at 660 km depth ($\gamma_{660} = -3$ MPa/°K) hinders the ascent of the plume, and it might be suspected that the entrainment of surrounding mantle may be enhanced as the plume head 'slows' down at the phase transition. This model differs from the standard model only in the introduction of phase changes; thus, the initial conditions (Fig. 6a and b) are identical to the ones previously described. Fig. 6c shows the plume head at the endothermic phase change. Although the head tends to flatten, the phase change does not have a large enough Clapeyron slope to represent a barrier to the ascent of the plume. The corresponding concentration field (Fig. 6d) shows that the degree of entrainment is not enhanced. In fact, within the plume head $C > 90\%$. The release of latent heat increases the potential temperature of the plume by ~ 20°C. However, the opposite effect occurs at the exothermic phase change, so that, globally, the net change in temperature is minor.

Fig. 6e shows that the plume head narrows as it rises through the exothermic phase change and the effect on the degree of entrainment is minor (Fig. 6f). The results of this model suggest that phase changes do not affect the degree of entrainment within the melting zone of the plume head. However, we observe that fringes of source material are introduced in the upper mantle even at great distance from the plume axis, as indicated in Fig. 6g and h. Fig. 7 shows the contours of the C-field and the melting region, when the total melt volume is ~ 3.2 × 10⁶km³. The bulk of the plume material partially melting is located in an area with high concentration of original source material. The corresponding lithospheric age for Fig. 7 is only 40–50 Myr, since in
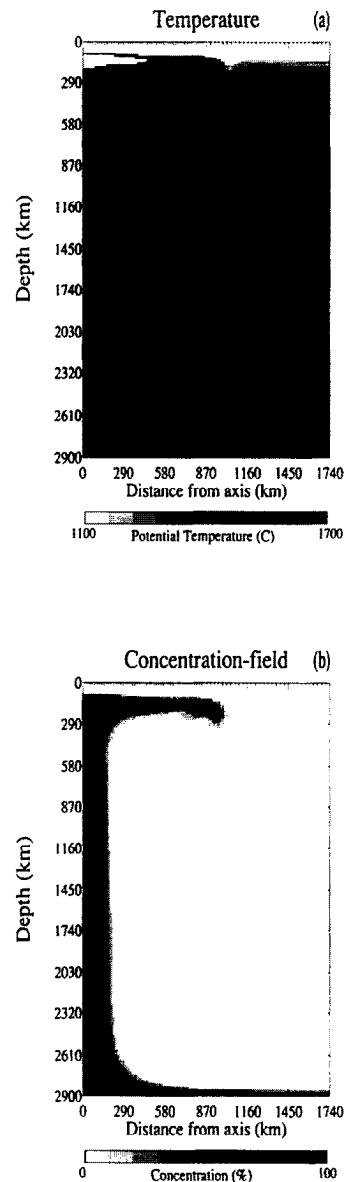
Fig. 8. Evolution of a plume for the model with mantle layered viscosity ($\eta_{lm} = 10^{22}$ Pa s, $\eta_{um} = 10^{21}$ Pa s). Top: the temperature field. (a) The plume is at sublithospheric depths, the melting zone is the white area beneath the lithosphere. Bottom: (b) the concentration field at the same elapsed time as the figure above. The scale for the C-field is from 0 to 100%. To show the temperature structure of the plume more clearly, the minimum potential temperature in the gray scale is 1100°C. This means that the lithosphere (where $T < 1100$°C) is depicted in white.

this model we prevent excessive cooling and thicken ing of the lithosphere by resetting the lithosphere's temperature to $T_{Pm} = 1300°C$, when the plume head is at 2500 km depth.

We have tested models with larger negative Clapeyron slopes at 660 km depth. For $\gamma_{660} = -4$ MPa/°K there is no qualitative difference in our results, while for $\gamma_{660} = -5$ MPa/°K the plume is stopped at 660 km depth, so that there is no melting in the plume. However, these extreme values are unlikely for mantle plumes, since the Clapeyron slope for peridotite mantle decreases to nearly zero at temperatures above 1800°C [31].

3.4. Model with mantle viscosity contrast

This model has a viscosity increase of 10 between upper and lower mantle, so that $\eta_{lm} = 10^{22}$ Pa s. The bottom temperature is the same as the previous cases (i.e., 1700°C). Because of the increased viscosity of the lower mantle, this model has a smaller heat flux through the boundary. This affects the time needed for the plume to form and, as in the previous model, we avoid excessive aging of the lithosphere by resetting the lithospheric temperature to 1300°C

when the plume head is at 2500 km depth. Fig. 8a and b show the temperature field and the C-field when the melt volume is $\sim 2 \times 10^6$ km^3, and the relation between the C-field and the melting region is shown in Fig. 9. We see again that, within the melting region, the concentration of original plume source material is above 80%.

4. Discussion

We have used a numerical model to investigate thermal entrainment in mantle plumes that originate from a thermal boundary layer in the deep mantle. In the last decade, the issue of entrainment for flow conditions appropriate to the mantle (at low Reynolds number, or infinite Prandtl number) has been investigated with laboratory experiments which have contributed significantly to our understanding of plume dynamics, but such experiments cannot quantitatively address partial melting processes. Our model overcomes these limitations by combining solid-state flow dynamics with a melting model. We trace the flow of an initial layer of material that is thermally buoyant and geochemically distinct from the overly-
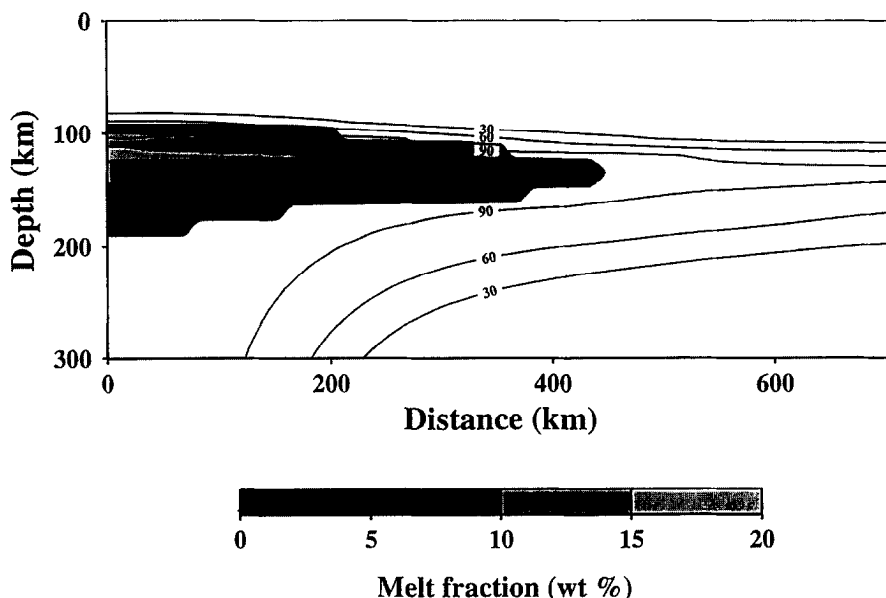

Fig. 9. Model with layered viscosity mantle: contours of the concentration field. The melting region is shaded.

ing mantle using a chemical field passively advected by the flow. It is beyond of the scope of this paper to define the geochemical signature of this layer in terms of possible geochemical reservoirs, or to address the origin of geochemical differences between the lower mantle and the boundary layer at the core–mantle boundary.

We have shown that a plume, generated by boundary layer instability and rising through the mantle, entrains only a small fraction of surrounding mantle into the region that undergoes partial melting. For the isoviscous case, the rim of surrounding mantle conductively heated by the plume remains confined to the periphery of the head. For the case with temperature-dependent viscosity (factor of 30 maximum contrast), the flow confines the original source material along the plume axis and in a torus-shaped volume. The confinement of source material to the plume axis and in a torus is in agreement with predictions of the similarity solutions by Griffiths [32] and with laboratory experiments [13]. However, in our model, the surrounding mantle flowing along the axis and within the base of the plume cap is only weakly stirred into the head during plume rise to the base of the lithosphere. It is possible that a more realistic rheology, with stronger temperature-dependent viscosity, may increase the 'stirring' within the plume head, and may cause more of the entrained material to be hot enough to melt. However, we have found that the factor of 30 temperature dependence of viscosity hardly increases the degree of entrainment relative to the isoviscous case.

We have also investigated models with layered mantle viscosity and with mantle phase transitions. We find some variations in the shape of the original source material in the plume head, but recirculation in the plume head and entrainment of surrounding mantle into the melting region are not strongly affected. For all the models both the ascent time of the plume in the mantle (approximately 30–40 Myr, once the thermal instability has formed) and the size of the plume head prior to sublithospheric spreading (approximately 500 km radius, for the 1500°C isotherm) are in agreement with values predicted by Griffiths and Campbell [13], for corresponding values of buoyancy flux and initial excess temperature.

We have quantified the proportion of entrained mantle and original source components present in the plume material undergoing partial melting. Including a melting model is particularly important because it allows us to test if the entrained mantle, which is heated by thermal conduction, is hot enough to cause partial melting. Only the plume material that partially melts generates volcanic products observable at the surface. In our models melting occurs within a radius of about 300 km of the plume axis, where the concentration of original source material exceeds 90%. This result seems to hold for a range of variations in mantle plume model parameters and it implies that thermally buoyant mantle plumes are not efficient in sampling the mantle through which they rise.

Our results may appear to be in conflict with Griffiths and Campbell's interpretation of their laboratory experiments, where it was concluded that magmas from mantle plume heads should reflect a large degree of entrainment of surrounding mantle [13]. However, there are four significant differences between our models:

First, the hottest part of a plume head is always that containing the highest concentration of original plume source material. In our models, only a relatively small fraction of the plume head undergoes partial melting, resulting in magmas that reflect a high concentration of source material. In contrast, Campbell and Griffiths [5] assumed that the entire plume head was sampled equally by the melting process.

Second, our plumes are generated from a boundary layer, so that the initial boundary layer instability ('head') is formed with a fairly smooth temperature gradient between the center of the head and the rim (e.g., Fig. 4c). This form is a consequence of feeding the plume from a boundary layer, which has a natural thermal gradient. In Griffiths and Campbell's experiments, the entire temperature contrast between initially injected plume material and surrounding fluid occurs across a boundary layer that is much thinner than the diameter of the plume head, because plume material is injected at a constant temperature. Thus, the rate of heat loss from the original plume material in our numerical experiments is much less than the heat loss from the dyed material in Griffiths and Campbell's experiments (probably by about a factor of $1/3$ — the ratio of boundary layer thickness to plume head radius). This reduced heat loss results in

a smaller rate of thermal entrainment of surrounding fluid in our calculations.

Third, our plume heads only rise a maximum of about 3 plume head diameters before they begin to flatten beneath the lithosphere. At that point, shear flow in the spreading plume head tends to 'unwrap' the torus of source material. This unwrapping further reduces the proportion of entrained material that undergoes partial melting. The laboratory experiments show that, after only 3 diameters of plume head rise there is little entrainment (Griffiths and Campbell [13], Fig. 1b), but the scaling of these experimental results to the mantle apparently involved at least 5 diameters of plume rise, resulting in more entrainment.

Fourth, our maximum mantle/plume viscosity contrast (limited by grid resolution) is only a factor of 30, whereas Griffiths and Campbell's plume source fluid was a factor of 300 less viscous than the surrounding tank fluid. Our calculations do not suggest that the degree of entrainment is a strong function of viscosity contrast and we think it unlikely that an additional factor of 10 in viscosity contrast will significantly enhance entrainment. (A larger viscosity contrast would further reduce the width of the plume tail, which would make our models more 'Earth-like'.)

We believe that the first three of these differences reflect a closer approximation in our models to the expected behavior of thermal plumes in the mantle: Our plumes develop from a thermal boundary layer, they rise through the mantle and spread beneath the lithosphere, and partial melting occurs only in the regions that are hot enough to melt. However, there is still a need to extend the models we have presented here to include a larger parameter range, especially a stronger temperature dependence of the viscosity.

Another limitation of our results is that we have modeled plumes that melt beneath the lithosphere, as opposed to plumes that cause large-scale lithospheric extension. In the latter case, higher melt fractions will be obtained in the plume source material, and more of the entrained mantle component will undergo melting, resulting in a large increase in total melt volume [12]. Because our models are axisymmetric, we cannot approximate the rifting process very well. However, a larger entrained mantle signa-

ture might result from magmas generated in a flood basalt event accompanied by a high degree of lithospheric extension.

Our results suggest that, if mantle plumes are generated as thermal instabilities at the core–mantle boundary, the material that undergoes partial melting at sublithospheric depths represents mainly the isotopic and trace element composition of material very near the core–mantle boundary. This conclusion does not, of course, preclude assimilation of lithospheric or crustal signatures into the geochemistry of primary magmas as they rise toward the surface. We suggest that, if flood basalts are geochemically heterogeneous, the heterogeneity is due mainly to inherent heterogeneity of the plume source region, lithospheric/crustal contamination, or perhaps both.

Acknowledgements

References

[1] W.J. Morgan, Convective plumes in the lower mantle, Nature 230, 42–43, 1971.

[2] W.J. Morgan, Plate motions and deep mantle convection, Mem. Geol. Soc. Am. 132, 7–22, 1972.

[3] W.J. Morgan, Hotspot tracks and the opening of the Atlantic and Indian Oceans, in: The Sea, vol. 7, The Oceanic Lithosphere, C. Emiliani, ed., pp. 443–487, Wiley, New York, 1981.

[4] M.A. Richards, R.A. Duncan and V.E. Courtillot, Flood basalts and hotspot tracks: Plume heads and tails, Science 246, 103–107, 1989.

[5] I.H. Campbell and R.W. Griffiths, Implications of mantle plume structure for the evolution of flood basalts, Earth Planet. Sci. Lett. 99, 79–93, 1990.

[6] M.A. Richards, D.L. Jones, R.A. Duncan and D.J. DePaolo, A mantle plume initiation model for the Wrangellia flood basalt and other oceanic plateaus, Science 254, 263–267, 1991.

[7] S.R. Hart, E.H. Hauri, L.A. Oschmann and J.A. Whitehead, Mantle plumes and entrainment: isotopic evidence, Science 256, 517–520, 1992.

[8] N.T. Arndt, G.K. Czamanske, J.L. Wooden and V.A. Fedorenko, Mantle and crustal contributions to continental flood volcanism, Tectonophysics 223, 39–52, 1993.

[9] M. Stein and A.W. Hofmann, Mantle plumes and episodic crustal growth, Nature 372, 63–68, 1994.

[10] N.T. Arndt and U. Christensen, The role of lithospheric mantle in continental flood volcanism: Thermal and geochemical constraints, J. Geophys. Res. 97, 10,967–10,981, 1992.

[11] S. Watson and D.P. McKenzie, Melt generation by plumes: A study of Hawaiian volcanism, J. Petrol. 12, 501–537, 1991.

[12] C.G. Farnetani and M.A. Richards, Numerical investigation of the mantle plume initiation model for flood basalt events, J. Geophys. Res. 99, 13813–13833, 1994.

[13] R.W. Griffiths and I.H. Campbell, Stirring and structure in mantle starting plumes, Earth Planet. Sci. Lett. 99, 66–78, 1990.

[14] R.W. Griffiths, Thermals in extremely viscous fluids, including the effects of temperature-dependent viscosity, J. Fluid Mech. 166, 115–138, 1986.

[15] M.A. Richards and R.W. Griffiths, Thermal entrainment by deflected mantle plumes, Nature 342, 900–902, 1989.

[16] E.H. Hauri, J.A. Whitehead and S.R. Hart, Fluid dynamic and geochemical aspects of the entrainment in mantle plumes, J. Geophys. Res. 99, 24275–24300, 1994.

[17] R.W. Griffiths and I.H. Campbell, On the dynamics of long-lived plume conduits in the convecting mantle, Earth Planet. Sci. Lett. 103, 214–227, 1991.

[18] K.E. Neavel and A.M. Johnson, Entrainment in compositionally buoyant plumes, Tectonophysics 200, 1–15, 1991.

[19] R.W. Griffiths, The differing effect of compositional and thermal buoyancies on the evolution of mantle diapirs, Phys. Earth Planet. Inter. 33, 304–317, 1986.

[20] L.H. Kellogg, Interaction of plumes with a compositional boundary at 670 km depth, Geophys. Res. Lett. 18, 865–868, 1991.

[21] U. Christensen, Mantle convection with active chemical heterogeneities, in: Crust/Mantle Recycling at Convergence Zones, S.R. Hart and L. Gulen, eds., pp. 183–189, 1989.

[22] A. Lenardic and W.M. Kaula, A numerical treatment of geodynamic viscous flow problems involving the advection of material interfaces, J. Geophys. Res. 98, 8243–8260, 1993.

[23] D.P. McKenzie and M.J. Bickle, The volume and composition of melt generated by extension of the lithosphere, J. Petrol. 29, 625–679, 1988.

[24] N.M. Ribe, Dynamical geochemistry of the Hawaiian plume, Earth Planet. Sci. Lett. 88, 37–46, 1988.

[25] G.F. Davies, Ocean bathymetry and mantle convection, 1. Large-scale flow and hotspots, J. Geophys. Res. 93, 10467–10480, 1988.

[26] N.H. Sleep, Hotspots and mantle plumes: Some phenomenology, J. Geophys. Res. 95, 6715–6736, 1990.

[27] D.L. Turcotte and G. Schubert, Geodynamics, 450 pp., Wiley, New York, 1982.

[28] J. Verhoogen, Phase changes and convection in the Earth's mantle, Philos. Trans. R. Soc. London Ser. A 258, 276–283, 1965.

[29] E. Ito and E. Takahashi, Ultra high-pressure phase transformations and the constitution of the deep mantle, in: High-Pressure Research in Mineral Physics, M. Manghnani and Y. Syono, eds., Am. Geophys. Union Geophys. Monogr. 34, 486 pp., 1986.

[30] F.M. Richter, Finite amplitude convection through a phase boundary, Geophys. J. R. Astron. Soc. 35, 265–276, 1973.

[31] T. Kato and M. Kumazawa, High pressure effect on the melting relation in the system Mg_2SiO_4–$MgSiO_3$: Phase transitions in the constituent phases and differentiation by melting in the Earth's mantle, in: Dynamic Processes of Material Transformation in the Earth's Interior, M. Marumo, ed., pp. 277–308, 1990.

[32] R.W. Griffiths, Particle motion induced by spherical convective elements in Stokes flow, J. Fluid Mech. 166, 139–159, 1986.

[33] C.-Y. Chen and F.A. Frey, Trace element and isotopic geochemistry of lavas from Haleakala volcano, East Maui, Hawaii: Implications for the origin of Hawaiian basalts, J. Geophys. Res. 90, 8743–8768, 1985.